Surface properties of spark-ablated metal oxide nanoparticles studied in-flight

Powder Technology 476 (2026) 122363

Contents lists available at ScienceDirect

Powder Technology

journal homepage: www.journals.elsevier.com/powder-technology

Surface properties of spark-ablated metal oxide nanoparticles studied in-flight☆

Linnéa Jönsson [a,b,*], Calle Preger [c], Thomas Krinke [a,b], Marie Bermeo [a,b], Mehran Sedrpooshan [b,f], Hajar Jalili [b,d], Mohammad Pourhossein [a,b], Bengt O. Meuller [b,e], Axel C. Eriksson [b,e], Jenny Rissler [b,e], Knut Deppert [a,b], Maria E. Messing [a,b,f]

[a] Department of Solid State Physics, Lund University, 221 00 Lund, Sweden
[b] NanoLund, Lund University, 221 00 Lund, Sweden
[c] MAX IV Laboratory, Lund University, Box 118, 221 00 Lund, Sweden
[d] Synchrotron Radiation Research, Lund University, Box 118, 221 00 Lund, Sweden
[e] Ergonomics and Aerosol Technology, Lund University, 22100 Lund, Sweden
[f] Quantum Device Physics Laboratory, Department of Microtechnology and Nanoscience, Chalmers University of Technology, 412 96 Gothenburg, Sweden

HIGHLIGHTS

- In-flight XPS reveals true nanoparticle surface oxide without deposition artifacts.
- Carrier gas composition controls NP surface chemistry during in-flight heating.
- Surface tuning of spark-ablated metal oxide NPs depends strongly on the material.
- Carrier gas and heating tune Sn and Zn surfaces, while Al remains highly stable.
- Size distributions reveal how spark energy and frequency control NP formation.

GRAPHICAL ABSTRACT

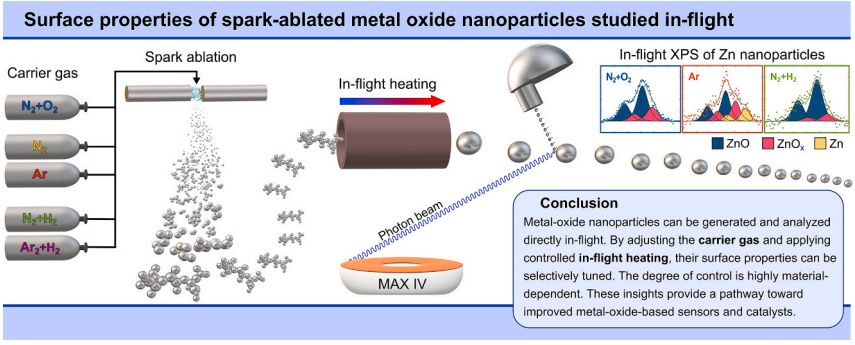

ARTICLE INFO

Keywords:
Metal oxide nanoparticles
In-flight
Carrier gas
Surface properties
Oxidation state
Spark ablation

ABSTRACT

Metal oxide nanoparticles are widely used in catalysis, photovoltaics, and gas sensing, where surface structure and oxidation state strongly influence performance. This work investigates how carrier gas composition, combined with in-flight heating, can be used to control the surface properties of metal oxide nanoparticles generated via the gas-phase method, spark ablation. Sn, Zn, and Al nanoparticles were characterized using in-flight X-ray photoelectron spectroscopy (XPS) at the MAX IV synchrotron radiation facility, enabling near real-time measurement of suspended particles under oxidizing ($N_2 + O_2$), inert (N_2 and Ar), and potentially reducing ($N_2 + H_2$ and $Ar + H_2$) gas environments, without introducing potential changes associated with particle deposition and storage. To support the interpretation of the XPS results, the particle size distributions, spark energy and frequency, and compaction behaviour were studied, providing insight into how material properties and generation conditions affect surface chemistry.

☆ This article is part of a Special issue entitled: 'Pratsinis' published in Powder Technology.

* Corresponding author at: Department of Solid State Physics, Lund University, 221 00 Lund, Sweden.
E-mail address: linnea.jonsson@ftf.lth.se (L. Jönsson).

https://doi.org/10.1016/j.powtec.2026.122363
Received 30 November 2025; Received in revised form 22 February 2026; Accepted 2 March 2026
Available online 7 March 2026

The XPS results show that for Sn nanoparticles, surface oxidation state can be tuned from SnO_2 to SnO and metallic Sn by selecting appropriate carrier gas and in-flight heating temperature. For Zn, the carrier gas primarily determines the surface composition, while heating has only a minor influence on the balance between ZnO, oxygen-deficient ZnO_x, and metallic Zn on the surface. In contrast, the surface oxide of Al nanoparticles remains largely unaffected by both carrier gas and in-flight heating. These findings demonstrate how careful control of carrier gas and in-flight thermal processing can be used to tailor nanoparticle surface properties, providing a pathway for designing materials optimized for specific applications.

1. Introduction

Owing to their size-, shape-, and composition-dependent properties, nanoparticles (NPs) are used in a wide range of applications, including catalysis, medical diagnostics, energy storage, and solar cells [1]. While crystalline noble metal NPs are often favoured for many applications, there is a high demand for metal oxide NPs, ranging from fully oxidized particles to those covered in a surface oxide that protects the core [2–4].

Metal oxide NPs of Sn, Zn, and Al are semiconductor materials with wide or ultrawide bandgaps, enabling their use in applications such as gas sensing, photocatalysis, and transparent conductive films for solar cells [5–7]. Their optoelectronic properties make them particularly attractive as catalysts for processes including wastewater treatment, organic pollutant degradation, and H_2 generation [8–10]. Furthermore, coupling these oxides with noble metals such as Au and Ag can promote interfacial charge transfer and significantly enhance catalytic activity [11–13].

For many applications, the surface properties of metal oxide NPs play a crucial role, as they directly influence particle reactivity. Both surface contamination and changes in surface oxidation state can affect particle properties in distinct ways. Therefore, the ability to tune the surface state is a key parameter in optimizing material performance for specific applications. For many metal oxide NPs, the oxidation state is established during production; thus, better understanding and control of oxidation during particle synthesis are essential.

Metal oxide NPs can be produced through various chemical methods, such as hydrothermal synthesis [14], sol-gel processing [2], and precipitation techniques [15]. However, these methods require chemical precursors or ligands that may introduce unwanted surface contamination. While post-processing can typically remove these contaminants, such steps are often costly, time-consuming, and may generate chemical waste. In contrast, physical gas-phase generation methods, such as flame spray pyrolysis and spark ablation, produce nanoparticles in a continuous flow of carrier gas, eliminating the need for chemical additives and largely avoiding post-processing surface cleaning [16,17]. Flame spray pyrolysis offers relatively high production rates, but its reliance on flammable metal-organic precursors limits material selection, and the presence of O_2 in the reactor can further restrict its use. These factors often make spark ablation a more versatile production route [10,18].

Spark ablation produces NPs via physical ablation and evaporation of atoms from two opposing conducting electrodes [19]. Generating multielement NPs is realized by using pre-alloyed or sintered electrodes, or by using electrodes consisting of two different elements. This makes spark ablation an extremely flexible method that allows tuning of NP composition [20–23]. Metal NPs are usually produced if the carrier gases used are inert (e.g., N_2 and Ar), and the materials are noble. So far, not much attention has been brought to examine their surface in detail immediately after production, before being exposed to the ambient atmosphere. It has been shown, though, that even tiny amounts of O_2 impurities in a high-purity gas like N_2 5.0 are enough to oxidize the surface of NPs of certain elements [24–26], and that extremely clean carrier gases (oxygen conc. 10^{-13} ppm) are needed to suppress oxidation of easily oxidated materials [27].

In spark ablation, as in many physical processes to generate nanoparticles, the particle oxidation depends not only on the material's susceptibility to oxidation and the purity of the carrier gas, but also on factors such as leakage of O_2 into the system or the presence of oxidized components on the setup's interior walls [28]. In contrast to noble metals like Au, Pt, and Pd, metals like Sn and Zn may still undergo oxidation due to impurities in the carrier gas, like trace oxygen or water vapor. To suppress oxidation, a small amount of H_2 can be added to the carrier gas. H_2 acts as a reducing agent when its affinity to react with O_2 species (and form H_2O) is higher than the affinity of the metal to react with O_2 species, and can hence prevent oxidation of some materials [24,29]. In combination with heat, reduction by H_2 has been shown to be efficient [30,31].

In-flight heating of NPs is a common technique in spark ablation and is typically employed after the spark generator to control the morphology and structure of the produced agglomerates. By allowing the suspended particles to pass through a furnace at a sufficiently high temperature, the agglomerates can compact into spherical particles [32,33]. Metal oxides typically have much higher melting points compared to their metallic counterparts, making full compaction more difficult to achieve. In-flight heating, combined with a specific gaseous environment, can also be used to tune the surface oxide of certain materials. Studies have shown that controlled in-flight heating of Sn nanoparticles in a hydrogen-containing carrier gas enables gradual reduction of surface oxides, thereby allowing precise tuning of the surface composition [30].

This work investigates how the choice of carrier gas and in-flight heating influence the surface composition of metal oxide NPs. To fully understand these processes, the measurements should be performed in-situ, while the particles are suspended in the carrier gas. Conventional characterization techniques, such as X-ray diffraction (XRD) and transmission electron microscopy (TEM), cannot easily provide detailed chemical analysis of a material's surface. X-ray photoelectron spectroscopy is surface-sensitive, but typically restricted to ex-situ measurements, where accurate analysis depends on the preservation of the sample's surface chemistry between generation and characterization, which might not be possible. To overcome this limitation, the present study employs in-flight XPS just after generation, which, to our knowledge, has only been applied to spark ablation-generated NPs a few times before [30,31,34], though the technique has been applied to study aerosols previously [35,36].

Results are presented for Sn, Zn, and Al nanoparticles generated in different carrier gases: oxidizing (N_2 + 21%O_2), inert (N_2 & Ar), and reducing (N_2 + 5%H_2 & Ar + 2.8%H_2). The particles' size distributions, morphology, and compaction behaviour are analysed, and their surface is examined using in-flight XPS at the MAX IV synchrotron facility in Lund, Sweden. By providing in-flight heating, the combined effects of carrier gas and temperature on the surface properties were systematically investigated.

2. Methods

2.1. Nanoparticle generation

Single-element metal oxide NPs were generated by spark ablation using electrodes of Sn (>99.99% purity), Zn (>99.99% purity), and Al (>99.95% purity), each 3 mm in diameter (Goodfellow GmbH). The electrodes were positioned approximately 1 mm apart. The spark was initiated by applying an electric field at breakdown voltage across the

gap using a high-voltage power supply (Technix, Model CCR15-P-750). Spark frequency and spark energy were determined by a 19 nF capacitor bank that was charged with a current of 5 mA. The carrier gas was introduced through the electrode gap at a flow rate of 2 L min^{-1}, regulated by a mass flow controller (MFC) (Bronkhorst, EL-FLOW®, EL-PRESS metal seal). For Ar-based gases, the flow was also set to 2 L min^{-1}, which is the instrument maximum. However, because the MFC was calibrated for N_2, the actual Ar flow was lower, approximately 1.4 L min^{-1}, consistent with the conversion factor that accounts for the differences in gas density and specific heat capacity [37].

When the applied voltage exceeds the breakdown threshold, the carrier gas forms a localized plasma, leading to spark discharge, electrode ablation, and evaporation of the electrode material [38]. The resulting vapor plumes are mixed within 20–25 μs after gas breakdown and rapidly cooled through adiabatic expansion [39]. The effective quenching (from ~20,000 K to 300 K) [40] of the vapor plume facilitates atomic nucleation and nanoparticle formation. Notably, this process can also yield alloyed nanoparticles if electrodes of different materials are used, even if the metals are immiscible in bulk [20,41]. Carrier gases employed included oxidizing (N_2 + 20.9% O_2, ≥ 99.9995% purity), inert (N_2, 99.99% purity; Ar, 99.999% purity) or reducing atmospheres (N_2 + 5% H_2; Ar + 2.8% H_2). An overview of the particle generation process and experimental setup is shown in Fig. 1.

2.2. Number size distribution & compaction behaviour

The number size distributions of NPs generated in different carrier gases were measured using a scanning mobility particle sizer (SMPS) (TSI, SMPS 3938 L76 with Soft-X-ray neutralizer 3088). The SMPS was operated with an aerosol flow of 0.3 L min^{-1} and a sheath gas flow of 6 L min^{-1}, which allows for measuring high particle concentrations without running the condensation particle counter (CPC) into high concentration error. Particle mobility diameters were scanned from 9.82 nm to 414.2 nm. The reported size distributions represent the average of three scans.

For some material–gas combinations, a high fraction of large particles (d_p > 414.2 nm) was observed. Because the SMPS setup lacked an impactor, which would have determined the upper size limit of particles entering the DMA, the multiple charge correction implemented in the TSI Aerosol Instrument Manager software could not be used. Instead, a data inversion algorithm was applied to the AIM raw data after applying a log-normal fit.

For the compaction study, a tandem DMA setup was employed, consisting of one DMA (TSI, model 3081), a custom-built Vienna-type DMA, and a tube furnace (Lenton, LTF) positioned between them. Agglomerates were first given a known charge distribution by a beta-emitting ^{63}Ni neutralizer, then size-selected at 70 nm with the first DMA. The particles were subsequently heated as they passed through the furnace with a residence time of approximately 5 s. After the furnace, the second DMA, coupled with an electrometer (TSI, model 3086 B), was used to measure the post-heating size distribution. The mode of this distribution was plotted as a function of furnace temperature, which directly gives information about the particles' compaction behaviour.

The DMAs and the DMA-electrometer setup was calibrated for N_2-based carrier gases. Therefore, for the size distribution and compaction studies, only N_2-based gases were included, as a reliable quantitative comparison with Ar-based gases would not have been possible.

2.3. Transmission electron spectroscopy

Particles were generated, size selected using a DMA, and deposited onto lacy carbon-coated copper grids with a custom-built electrostatic precipitator. The samples were stored and transferred under ambient conditions before TEM analysis (JEOL, 3000F). Because the agglomerates had low mass contrast and consisted of loosely connected primary particles forming large, open structures, careful imaging procedures were required, especially at higher magnifications. Prolonged electron-beam exposure altered the surface structure and dendritic morphology, so lower magnifications and short exposure times were used to minimize beam-induced changes and preserve the native particle characteristics.

2.4. In-flight XPS

The spark ablation setup was transported to the MAX IV synchrotron radiation facility (Lund, Sweden), where particles were generated as described above and introduced into the aerosol sample-delivery system at the gas-phase end station of the FinEstBeAMS beamline [34]. This system delivers aerosol particles from near-atmospheric pressure into a vacuum chamber in a continuous flow and focuses them into a narrow, highly concentrated particle beam. Aerosols entered the system through a 140 μm critical orifice at a constant mass flow of 0.088 L min^{-1}, passed

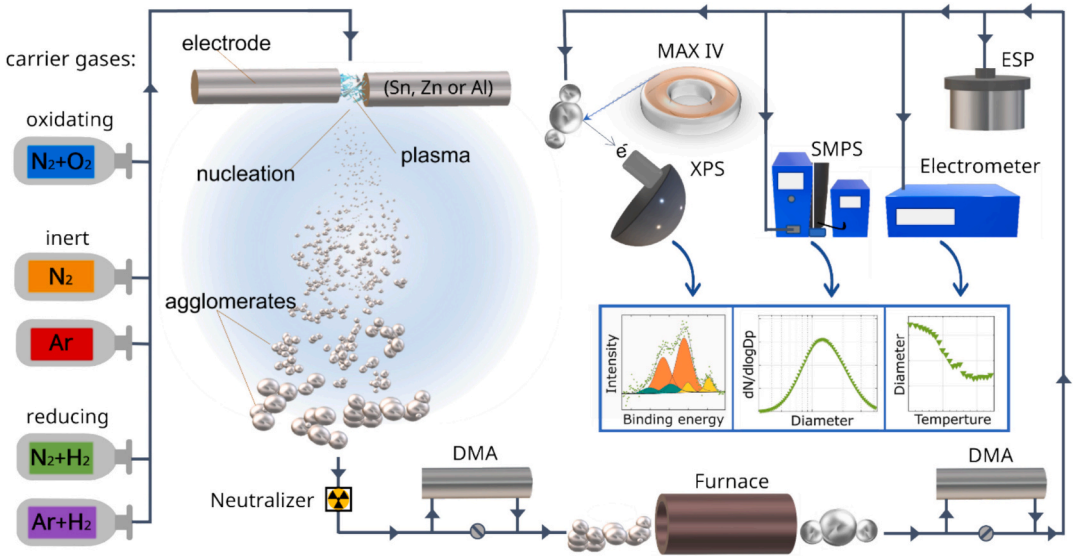

Fig. 1. A carrier gas was used to transport NPs generated from Sn, Zn, or Al electrodes via spark ablation. The resulting aerosol could then be directed through different experimental pathways: size selection using differential mobility analysers (DMAs), in-flight heating in a tube furnace, deposition onto a substrate in an electrostatic precipitator (ESP), particle counting with an electrometer or scanning mobility particle sizer (SMPS), or surface analysis using in-flight XPS at the MAX IV synchrotron. Through these approaches, particle compaction behaviour, size distribution, and surface composition were investigated.

through a relaxation tube, and were then collimated by an aerodynamic lens (Aerodyne PM1). The focused particle beam entered the vacuum chamber through a 1 mm conical skimmer, where it intersected with the photon beam.

The elliptically polarizing undulator was tuned to produce vertically polarized light, optimizing signal intensity with the vertically oriented electron analyzer (SCIENTA R4000). Since FinEstBeAMS provides its highest photon flux at relatively low photon energies, photon energies between 104 and 180 eV were selected depending on the material and probed orbitals. To achieve high surface sensitivity, photoelectrons with kinetic energies of ~70 eV were collected. Individual spectra were acquired over 10–60 min, depending on the signal strength, which varied with aerosol generation conditions.

At the photon energies used in these experiments, the inelastic mean free path of the photoelectrons was 0.5–0.6 nm (Sn: 104 eV, Zn: 180 eV, Al: 150 eV) [42]. Energy calibration relative to the vacuum level was performed using the binding energy of the outermost valence orbitals of N_2 at 15.58 eV [43]. Data analysis and spectral fitting were conducted using CasaXPS software [44].

2.4.1. Fitting of the Sn 4d photoelectron spectra

Shirley backgrounds and contributions from background gas were subtracted from the measured Sn 4d spectra. The spin-orbit components were fitted using Gaussian/Lorentzian sum functions with an area ratio of 3:2 and a fixed splitting of 1.1 eV. The relative peak positions were constrained such that Sn^{4+} was located 0.7 eV above Sn^{2+} and 2.0 eV above Sn^0. The full width at half maximum (FWHM) was restricted to 0.9–1.45 eV for Sn^{4+} and Sn^{2+}, and 0.5–0.6 eV for Sn^0 [30,34,45].

2.4.2. Fitting of the Zn 3p photoelectron spectra

Shirley backgrounds were subtracted from the XPS data, and the Zn 3p doublets ($3p_{½}$ and $3p_{3/2}$) were fitted using Gaussian/Lorentzian sum functions with an area ratio of 2:1 and a fixed spin-orbit splitting of 2.7 eV. The relative peak positions were constrained such that Zn^{2+} was located 1.5 eV above Zn^+ and 3.0 eV above Zn^0. The FWHM was restricted to 1.6–1.9 eV for the Zn^{2+} and Zn^+ doublets, and 1.3–1.5 eV for the Zn^0 doublets. The inclusion of Zn^+ in the fitting, despite its general classification as an unstable oxidation state, is justified and further discussed in the Results and Discussion, Section 3.3.2.

2.4.3. Fitting of the Al 2p photoelectron spectra

A linear background was subtracted from the Al 2p spectra, and the doublets were fitted using Gaussian/Lorentzian sum functions with an area ratio of 2:1, a fixed spin-orbit splitting of 0.44 eV, and FWHM values constrained between 1.35 and 1.65 eV [34,46]. Although the spin-orbit splitting of Al 2p is small and sometimes modelled with a single peak, fitting with doublets is generally considered more accurate [47].

3. Results & discussion

To investigate how the carrier gas influences the surface properties of metal oxide NPs, we first characterized their size distribution, morphology, and compaction behaviour in N_2-based carrier gases before performing in-flight XPS. For the in-flight XPS experiments, Ar-based gases were also used. Ar provides an inert reference environment and enables direct comparison with N_2-based gases without introducing nitrogen chemistry, offering a way to isolate the effect of nitrogen.

3.1. Size distributions and TEM analysis

Fig. 2 presents the size distributions of Sn, Zn, and Al nanoparticles generated in $N_2 + H_2$, N_2, and $N_2 + O_2$. All the material-gas combinations exhibit modes (size distribution peak positions) between 100 and 250 nm. For Sn and Zn (Fig. 2a and b), the largest modes occur in $N_2 + O_2$, the smallest in $N_2 + H_2$, and N_2 yields intermediate sizes. In contrast, Al (Fig. 2c), shows nearly identical mode diameters for all gases, although particle concentrations are highest in $N_2 + H_2$, followed by N_2 and then $N_2 + O_2$.

Note that for the size distribution measurements, the same electrode diameter, electrode gap, carrier gas flow, capacitance, and charging current were used. However, the voltage and frequency varied between both gases and materials, influencing the size distributions. The average voltage $\overline{U}$ was used to approximate the energy per spark as $E_s \approx 2C\overline{U}^2$, where C is the capacitance. The right panel in Fig. 2 presents the energy per spark versus average frequency for d) Sn, e) Zn, and f) Al in different carrier gases. A more accurate estimation of the energy dissipated in the electrode gap can be obtained by measuring and integrating the current waveform and the electrical resistance [48], which has been shown to be about 78%–85% of the estimated stored energy [49]. For the purpose here of relating the particle size distributions to the energy input to the electrode gap, the estimated average spark energy is good enough for a qualitative discussion. Another common way of correlating the energy

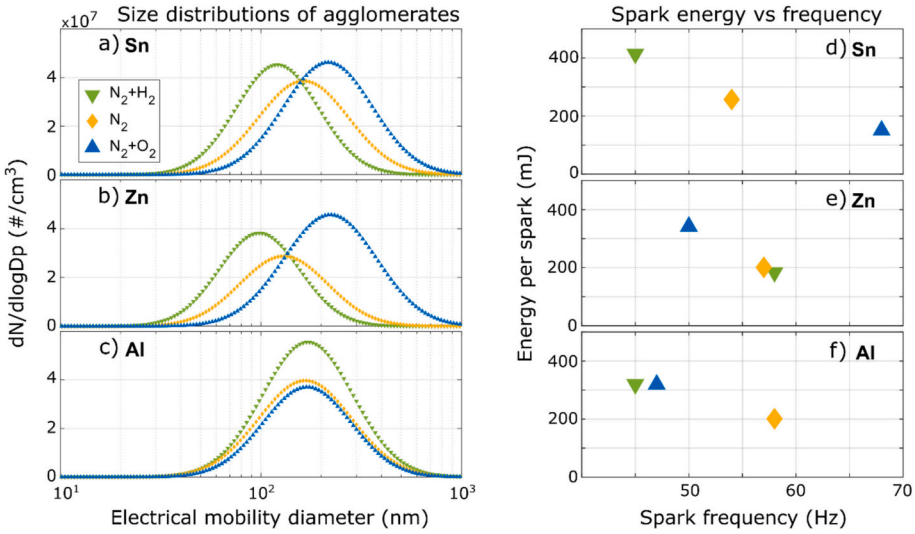

Fig. 2. Left panel: Size distributions of NP agglomerates generated from a) Sn, b) Zn, and c) Al electrodes using $N_2 + H_2$ (green▽), N_2 (yellow ⋄), and $N_2 + O_2$ (blue △), as carrier gases. Right panel: Energy per spark versus the spark frequency during the generation of d) Sn, e) Zn, and f) Al agglomerates in the same three gases. (For interpretation of the references to colour in this figure legend, the reader is referred to the web version of this article.)

per spark with the material output is to use gravimetry to estimate the material loss from the electrodes [50].

At first glance, the energy per spark versus frequency panel in Fig. 2 shows no universal trend across gases and materials. However, some patterns can be noted. N_2 is the most stable carrier gas, with spark energies ranging from 200 to 260 mJ and frequencies between 54 and 57 Hz for all three materials. In contrast, $N_2 + H_2$ and $N_2 + O_2$ exhibit larger material-dependent variations. For $N_2 + H_2$, the spark energy spans from ~200 mJ for Zn, ~300 mJ for Al, to ~400 mJ for Sn, with frequencies between 45 and 58 Hz. For $N_2 + O_2$, the spark energy ranges from ~150 mJ for Sn, ~320 mJ for Al, to ~350 mJ for Zn, accompanied by the widest frequency range (47–68 Hz).

In general, a high energy per spark in combination with a high frequency should lead to more ablated material. More material in the electrode gap can lead to either the formation of high particle number concentration, large agglomerate sizes, or large primary particles, or a combination thereof, depending on material and carrier gas properties. In other words, it may not be straightforward to correlate the size distributions with the energy per spark and frequency, since there are many parameters involved. To assist with the analysis, the morphology and structure of deposited agglomerates were examined using TEM. Before imaging, the particles were exposed to and stored in ambient air, likely resulting in surface oxidation, in contrast to the in-flight conditions for XPS. Fig. 3 presents TEM images of Sn, Zn, and Al agglomerates produced in different carrier gases, $N_2 + O_2$ (blue), N_2 (orange), and $N_2 + H_2$ (green).

All agglomerates shown in Fig. 3 exhibit a dendritic-like morphology, consisting of primary particles connected through varying degrees of necking. Since the particles were size-selected prior to deposition and TEM analysis, the average agglomerate size from Fig. 2 cannot be inferred from these images. Instead, the TEM analysis allows for comparison of the average primary particle size, which is important for interpreting the relationship between spark energy and the resulting size distributions.

For Sn, the estimated energy per spark is more than twice as high in $N_2 + H_2$ compared with $N_2 + O_2$, directly opposite to what would be expected from the size distributions in Fig. 2a. Although the spark frequency is lower in $N_2 + H_2$ (~45 Hz) than in $N_2 + O_2$ (~68 Hz), the large difference in spark energy should be the dominant factor influencing the amount of material ablation. Thus, the frequency alone is unlikely to explain why $N_2 + H_2$ shows higher spark energies while $N_2 + O_2$ still produces larger agglomerates at similar number concentrations. To understand this discrepancy, the primary particle size and composition must be considered, as these cannot be inferred from the agglomerate size distributions alone. For Sn, the TEM images in Fig. 3a, d), and g) suggest that the largest primary particles are formed in $N_2 + H_2$. To confirm this, a more detailed analysis of 50 primary particles across multiple agglomerates was performed (Fig. S1). The results show that $N_2 + H_2$ produces the largest primary particles (10.2 nm), followed by $N_2 + O_2$ (7.2 nm) and N_2 (6.6 nm). A plausible explanation is that although more material is ablated in $N_2 + H_2$ due to the higher spark energy, the particles coalesce more efficiently, forming larger primary particles. In contrast, when more oxygen is present, and Sn oxides form, the primary particles remain small and do not coalesce as effectively, which may also lead to the formation of larger overall agglomerates.

Fig. 2b shows that for Zn, production in $N_2 + O_2$ yields both the highest number concentration and the largest agglomerate size. This is consistent with Fig. 2e, where $N_2 + O_2$ gives the highest estimated spark energy, although it also exhibits the lowest spark frequency among the three gases. Comparing $N_2 + H_2$ and N_2, Zn produced in $N_2 + H_2$ reaches the highest number concentration, while N_2 results in slightly larger agglomerate diameters. This is reasonable given that the spark energies and frequencies for these two gases are nearly identical, leading to similar material production but differences in how the Zn material agglomerates. The largest average primary particle size is observed when the particles are generated in $N_2 + H_2$, as visible by comparing the TEM images in Fig. 3b), e), and h).

Fig. 2c shows that Al reaches its highest particle number concentration when produced in $N_2 + H_2$. However, this trend cannot be explained by the estimated spark energy (Fig. 2f), where $N_2 + H_2$ and $N_2 + O_2$ give nearly identical and the highest spark energies for Al. The spark frequencies for these two gases are also almost the same, meaning neither parameter accounts for the observed differences in size distribution. The size distributions for Al generated in N_2 and $N_2 + O_2$ are nearly identical, despite the higher spark energy in $N_2 + O_2$. The average primary particle size appears largely unchanged across the three carrier gases, based on TEM images in Fig. 3c), f), and i). This indicates rapid and complete oxidation of Al during generation, suppressing coalescence and limiting primary particle growth regardless of atmosphere. A plausible explanation of the difference in amount of material ablated is

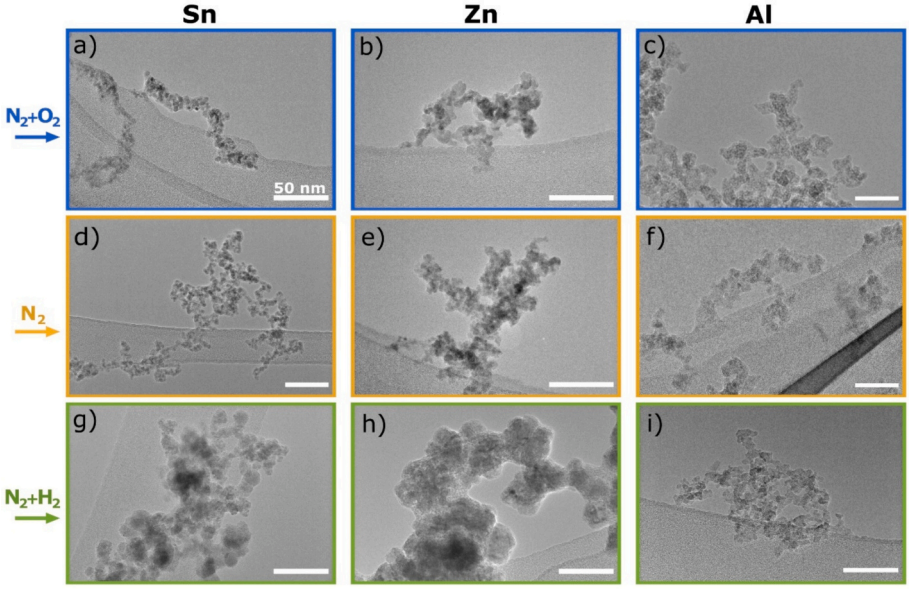

Fig. 3. TEM images of agglomerates generated from Sn, Zn, and Al electrodes in $N_2 + O_2$ (a-c: blue), N_2 (d-f: orange), and $N_2 + H_2$ (g-i: green). All scale bars are 50 nm. (For interpretation of the references to colour in this figure legend, the reader is referred to the web version of this article.)

that the electrode surfaces may be more oxidized during generation in $N_2 + O_2$ compared with N_2. Producing the same amount of material from a more oxidized surface requires more energy, which could lead to the observed trends in particle number concentration and agglomerate size.

Previous studies have shown that the choice of carrier gas has a strong impact on nanoparticle size, concentration, and production rate in spark ablation. For example, when using $N_2 + O_2$, N_2, and Ar, the breakdown voltage at a fixed electrode gap was similar for $N_2 + O_2$ and N_2, but approximately half in Ar. The higher breakdown voltages in the N_2-based gases led to increased material evaporation and resulted in larger primary particle sizes for Au agglomerates compared with Ar [50]. Comparable trends have been reported for transferred arc generation, where N_2 produced the highest mass yield, followed by $N_2 + H_2$ and then Ar [51]. These observations align well with our results for Sn and Zn nanoparticles: N_2 produced intermediate particle sizes, $N_2 + H_2$ yielded slightly smaller particles, and $N_2 + O_2$ generated the largest particles. In contrast, Al nanoparticles showed minimal sensitivity to the carrier gas. This difference likely reflects the intrinsic material properties, and specifically the strong oxygen affinity of Al, which most likely leads to fully oxidized particles regardless of the carrier gas used.

The detailed TEM analysis is essential to assess agglomerate structure and primary particle size, assisting in explaining the correlation between spark energy and particle production. With this improved understanding of the particle morphology when produced in different gases, the following section examines the compaction behaviour of the agglomerates during in-flight heating. The knowledge of the primary particle size will aid the interpretation of their restructuring and densification processes.

3.2. Compaction behaviour

To understand how in-flight heating influences particle surface properties, the compaction behaviour of agglomerates in different carrier gases was investigated. Previous studies have shown that even trace levels of impurities or oxygen delay compaction by increasing the required time or temperature, whereas adding reducing species such as H_2 accelerates restructuring [32,52,53]. Compaction is typically observed as a decrease in mobility equivalent diameter with increasing temperature until the particles reach full compaction, and the mobility diameter plateaus.

The compaction temperature of NPs is linked to, but generally lower than, the bulk melting point of the material, and it also depends on factors such as primary particle size and surface cleanliness. As a result, compaction behaviour can offer insight into particle composition, especially when the bulk melting points of expected constituents are known. Most nanoparticles compact between roughly one-third and one-half of their bulk melting point (in Kelvin) [54]. Because metal oxides usually have much higher melting points than their corresponding metals, the observed compaction temperature can indicate the relative amounts of metal and oxide present. Table 1 summarizes the melting points of Sn, Zn, Al, and their common oxides for comparison.

Fig. 4 shows the compaction of 70 nm size-selected agglomerates of Sn, Zn, and Al produced in $N_2 + O_2$ and $N_2 + H_2$ as the in-flight furnace temperature is increased from room temperature to 1200 °C. A general trend observed for all three elements in Fig. 4 is that particle compaction is more efficient in $N_2 + H_2$ than in $N_2 + O_2$, suggesting that carrier gas influences particle morphology and/or oxidation state. Nevertheless, each material exhibits its own distinct compaction behaviour. Note that data could not be collected for Sn and Zn in $N_2 + O_2$ at the highest temperatures due to thermal charging effects within the furnace [55]. For Zn in $N_2 + H_2$, no particle mode could be detected at temperatures above ~900 °C, probably due to complete evaporation in the furnace [56,57].

3.2.1. Compaction of Sn

For Sn nanoparticles in $N_2 + H_2$, no further decrease in mobility diameter is observed above ~800 °C, indicating full compaction at around 27 nm. This agrees with earlier studies [24,30] and is confirmed by TEM analysis of particles heated in-flight to 1100 °C (Fig. 4a, inset). The relatively high compaction temperature, far above the bulk melting point of Sn (234 °C), suggests that the particles remain at least partially oxidized even when produced in a reducing atmosphere.

In $N_2 + O_2$, the mobility diameter levels off near 50 nm below 1000 °C, but since no data were collected above this temperature, this apparent plateau is unlikely to represent full compaction. TEM imaging of particles heated to 800 °C in $N_2 + O_2$ shows that compaction is not achieved (Fig. 4a, inset), consistent with previous observations that Sn in N_2 does not fully compact even at 900 °C [24]. The small decrease in mobility diameter (from 70 nm to ~50 nm) supports the conclusion that full compaction is not reached at 1000 °C.

3.2.2. Compaction of Zn

Zn, like Sn, is known for having a low melting point. But Zn also has high vapor pressure, causing it to quickly evaporate at elevated temperatures [57]. This behaviour is evident for Zn nanoparticles generated in $N_2 + H_2$, where heating above ~700 °C causes the mobility mode diameter to drop below 20 nm, and even below 10 nm, without reaching a plateau (Fig. 4b, green). This strong size reduction is consistent with pronounced evaporation rather than compaction. TEM images of Zn particles generated in $N_2 + H_2$ and heated in-flight up to 600 °C (Fig. S2) also show noticeably smaller agglomerates, supporting the conclusion that evaporation dominates over compaction at elevated temperatures.

Zn generated in $N_2 + O_2$ shows clear compaction behaviour. TEM analysis of particles heated to 1100 °C in this gas (Fig. 4b, inset) confirms a compact morphology. This likely reflects the formation of Zn oxides during generation in $N_2 + O_2$, which suppresses Zn evaporation and allows compaction to proceed.

3.2.3. Compaction of Al

Al nanoparticles in both $N_2 + H_2$ and $N_2 + O_2$ show a gradual, nearly linear decrease in mobility diameter with increasing temperature, reaching 48 nm in $N_2 + H_2$ and 57 nm in $N_2 + O_2$ at the maximum furnace temperature of 1200 °C. In $N_2 + H_2$, a plateau slightly below 50 nm appears above ~1000 °C (Fig. 4c, green). The absence of compaction below the melting point of bulk Al (660 °C) indicates that the particles are at least partially oxidized even in the reducing $N_2 + H_2$ atmosphere. This interpretation is supported by TEM imaging of Al heated to 1100 °C (Fig. 4c, inset), and at 20 °C, 500 °C, and 900 °C in Fig. S3, which shows incomplete restructuring. Since Al_2O_3 is highly thermally stable, the apparent plateau could be caused by the formation of an oxide shell on the surface of the primary particles, which inhibits surface diffusion and slows coalescence. Moreover, mobility diameter is relatively insensitive to internal densification, so structural changes that occur without large changes in external shape may not significantly affect the measured mobility size.

Table 1
Melting points of bulk Sn, Zn, Al, and some of their common oxides.

Material	Sn	SnO	SnO_2	Zn	ZnO	Al	Al_2O_3
T_M (°C)	234	1080	1630	420	1975	660	2072

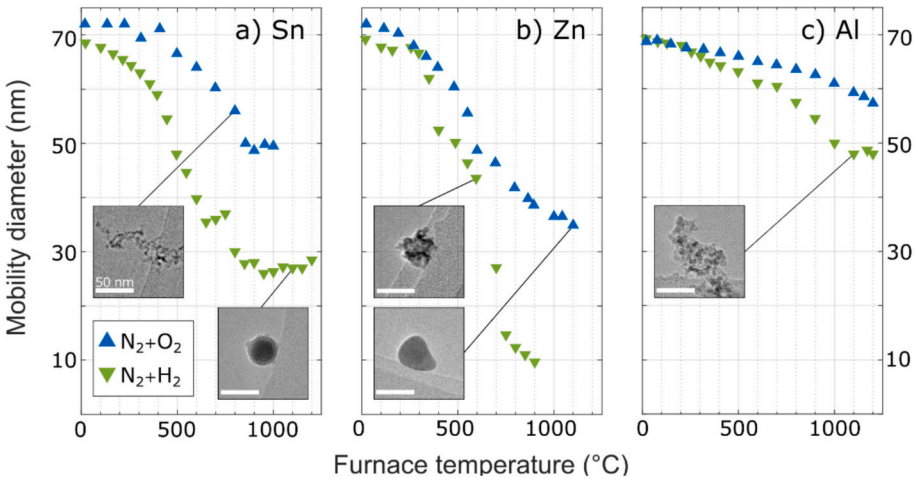

Fig. 4. Compaction behaviour of 70 nm nanoparticles of a) Sn, b) Zn, and c) Al generated in $N_2 + O_2$ (blue △) and $N_2 + H_2$ (green ▽) and heated in-flight. Insets show TEM images of the particle morphology in certain conditions. All TEM scale bars are 50 nm. (For interpretation of the references to colour in this figure legend, the reader is referred to the web version of this article.)

3.3. *In-flight XPS*

Up to this point, the carrier gases discussed have been N_2-based. In the in-flight XPS measurements, Ar-based carrier gases were also included. Due to time constraints of the beamtime campaign, priority was given to investigating how chemically distinct carrier gas environments—specifically oxidizing and reducing conditions introduced by O_2 and H_2—affect the particle surface chemistry. Pure N_2 was expected to result in a surface chemistry somewhere in between that of $N_2 + O_2$ and $N_2 + H_2$, and therefore not included. Although a direct comparison between pure N_2 and pure Ar would have enabled a clearer assessment of nitrogen-specific effects, such as potential nitridation, this was not the primary objective of the study.

For both Sn, Zn, and Al particles, the difference between their surface in $N_2 + O_2$ and $N_2 + H_2$ was studied. In addition, Ar was used for Sn and Zn, while for Al, known to oxidize very easily, $Ar + H_2$ was chosen to possibly reduce the oxidation and avoid nitride formation.

Fig. 5 provides an overview of the in-flight XPS results for Sn, Zn, and Al agglomerates without any in-flight heating. For each material, data for particles generated in different carrier gases were fitted, and the envelopes of those fits are displayed (detailed fitted spectra will be presented later). Clear shifts in peak positions and shapes are observed depending on the carrier gas. As expected, particles generated in $N_2 + O_2$ display peaks at higher binding energies than those generated in $N_2 + H_2$, consistent with the higher binding energies of oxides. For Sn and Zn generated in Ar, and for Al generated in $Ar + H_2$, the peaks appear at intermediate binding energies between the $N_2 + O_2$ and $N_2 + H_2$ cases, suggesting surface chemistries that differ from both the more oxidizing and more reducing N_2-based carrier gases.

Comparing the Sn spectra in Fig. 5a, the peak obtained in Ar closely resembles that in $N_2 + O_2$, with both showing a shoulder on the high–binding-energy side. In contrast, the $N_2 + H_2$ spectrum exhibits shoulders on both sides. Preliminary fits indicate that $N_2 + H_2$ requires roughly equal contributions of SnO_2 and SnO, $N_2 + O_2$ is best described by predominantly SnO_2, and Ar yields an intermediate mix of SnO_2 (~75%) and SnO (~25%).

For Zn (Fig. 5b), each carrier gas produces a distinctly different peak shape. All spectra show a shoulder on the higher binding energy side, and the Ar spectrum also shows an additional pronounced shoulder. Unlike typical Zn 3p fitting, which often includes only ZnO and metallic Zn, satisfactory fits here required Zn^{2+} (ZnO), Zn^{+} ($ZnO_{0.5}$), and Zn^0 (Zn). Further justification for this fitting approach is provided in Section 3.3.2.

For Al (Fig. 5c), the peak shapes are similar but clearly shifted depending on carrier gas: $N_2 + O_2$ appears ~1 eV higher in binding energy than $N_2 + H_2$, with $Ar + H_2$ falling between the two. This trend mirrors the shifts seen for Sn and Zn and is attributed to changes in electronic work function rather than oxidation state, and will be elaborated on more in Section 3.3.3.

Because the in-flight XPS is performed on aerosol particles without a substrate, the apparent binding energies are strongly influenced by the particle work function. Aerosol photoemission studies show that work function shifts can arise from differences in oxidation, as well as adsorption of gas-phase species [26]. Thus, the ~1 eV shifts observed

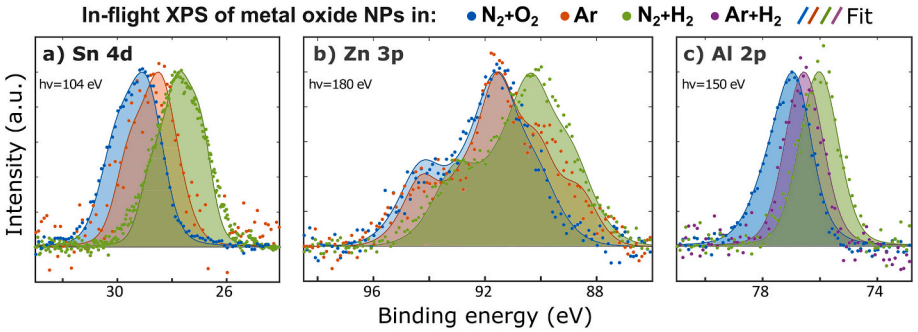

Fig. 5. In-flight XPS spectra of nanoparticle agglomerates generated from a) Sn, b) Zn, and c) Al electrodes in carrier gases of $N_2 + O_2$ (blue), Ar (red), $N_2 + H_2$ (green) and $Ar + H_2$ (purple). Clear differences in both peak position and shape are observed depending on the carrier gas. (For interpretation of the references to colour in this figure legend, the reader is referred to the web version of this article.)

here, particularly for Sn and Al, primarily reflect carrier-gas-dependent changes in surface electronic structure rather than differences in oxidation state. The following sections provide a detailed analysis of the element-specific spectra, showing the nanoparticles' surface properties in different carrier gases and under in-flight heating.

3.3.1. Sn

For Sn particles generated in $N_2 + O_2$, in-flight heating produced no major changes in the Sn 4d spectra (Fig. S4), indicating that the surface remained dominated by SnO_2. In contrast, heating Sn particles in $N_2 + H_2$ resulted in pronounced changes in both morphology and surface composition, as shown in Fig. 6, which combines TEM images with fitted in-flight XPS spectra. At room temperature (Fig. 6a), the particles appear as loosely bound agglomerates with primary particles around 10 nm. At 500 °C (Fig. 6b), the primary particles have coalesced into fewer but larger units, and at 1100 °C (Fig. 6c), they are fully compacted into nearly spherical particles with diameters of 50–70 nm (see Fig. S5 for low magnification overview).

The morphological transitions are accompanied by clear shifts in the Sn 4d surface oxidation state (Fig. 6d-f). At room temperature, the spectra require comparable contributions from Sn^{4+} and Sn^{2+}. At 500 °C, Sn^{2+} becomes dominant. At 1100 °C, a metallic Sn^0 component has appeared, while the Sn^{4+} fraction becomes small. The reduction of Sn oxides in $N_2 + H_2$ is consistent with previous reports showing the emergence of metallic Sn on the nanoparticle surface above ~900 °C [30,58].

TEM images of the particles heated to 1100 °C (Fig. 6c) show a core-shell structure, with a dense metallic core enclosed by an oxide shell. Because the TEM samples were deposited and stored under ambient conditions, one possibility is that the oxide shell formed after heating, during exposure to air. However, the in-flight XPS data show that both metallic Sn and Sn oxide are present on the surface during generation. Furthermore, increasing the heating temperature from 900 °C to 1100 °C, where the particles are known to be fully compact (Fig. 4), did not increase the metallic Sn surface fraction (Fig. S6). Together, these observations support an alternative explanation: the particles may become fully compact and almost fully reduced inside the furnace, but an oxide shell forms after they leave the hot zone and cool toward room temperature, when reduction by H_2 is no longer favourable, yet the particles remain airborne.

These results indicate that simply raising furnace temperature or increasing residence time is not an effective strategy for enhancing the metallic Sn surface fraction. Instead, controlling the carrier gas composition, such as increasing H_2 content or minimizing oxygen impurities, is likely a more effective route for tuning the surface chemistry of Sn nanoparticles. A detailed analysis of the primary particle size and its evolution with in-flight heating temperature in different carrier gases, and how these changes correlate with surface composition, would be a valuable direction for future work.

3.3.2. Zn

Fig. 7 shows the Zn 3p XPS spectra of Zn nanoparticles generated in different carrier gases and heated in-flight to 20, 300, and 600 °C. As noted earlier, the detection of Zn^+ is uncommon in the XPS literature because Zn + is unstable under ambient conditions [59,60]. However, oxygen-deficient ZnO, often denoted ZnO_x ($1 > x > 0$), Zn-rich ZnO, or ZnO with oxygen vacancies, is widely reported and is associated with green photoluminescence [61–63] and enhanced photocatalytic activity [7,64]. Coexistence of ZnO and ZnO_x has previously been confirmed via XPS and Auger peak spectroscopy [11,60], although, to our knowledge, no prior study has explicitly reported simultaneous Zn^{2+}, Zn^+, and Zn^0 within the same sample. This makes the interpretation of the present spectra both challenging and scientifically interesting. For simplicity in the fits, the x in ZnO_x is fixed as $x = 0.5$ to represent an oxygen-deficient oxide, although the actual vacancy concentration is not known.

For Zn produced in $N_2 + O_2$ (Fig. 7a-c), the spectra consistently contain both Zn^{2+} and Zn^+, and the relative contributions remain essentially unchanged with heating, even though particle restructuring is known to occur. When Ar is used as the carrier gas (Fig. 7d & e), all three oxidation states, Zn^{2+}, Zn^+, and Zn^0, are detected. Although Ar is inert, trace oxygen impurities are expected to oxidize Zn, so the presence of metallic Zn is notable. Further heating in Ar does not significantly alter the surface composition. For Zn particles generated in $N_2 + H_2$, the surface contains both Zn^{2+} and Zn^+, and in similar proportions as those in $N_2 + O_2$. Increasing the temperature shifts the distribution slightly toward higher oxidation states, with Zn^{2+} increasing and Zn^+ decreasing.

Note that the Zn 3p peaks from Zn particles generated in $N_2 + H_2$

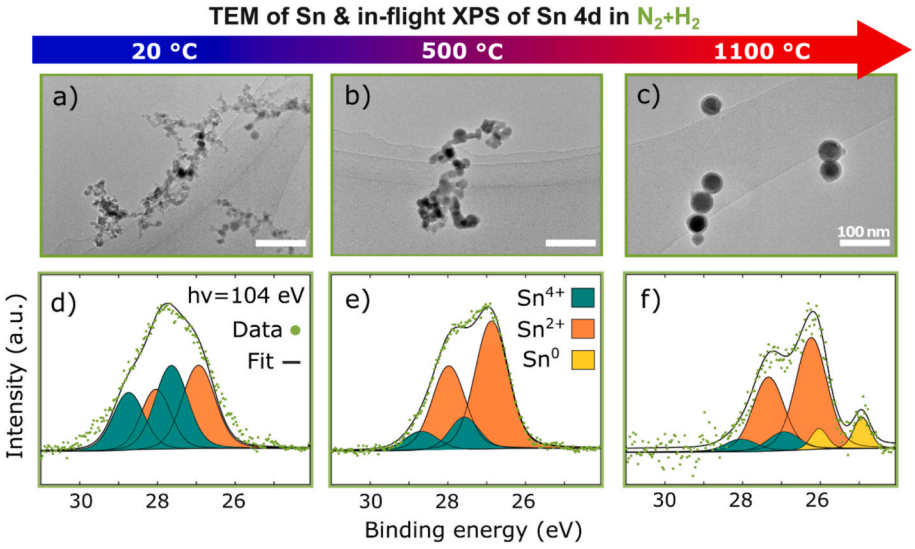

Fig. 6. Sn nanoparticles generated by spark ablation of Sn electrodes in $N_2 + H_2$ and heated in-flight, analysed using TEM (a-c) and in-flight XPS of the Sn 4d photoelectron spectra (d-f). As the particles are heated at 20 °C (a, d), 500 °C (b, e), and up to 1100 °C (c, f), both morphology and surface composition evolve. TEM images show a transition from loosely bound agglomerates to compact spherical particles, while XPS reveals changes in surface chemistry with varying contributions of SnO_2 (green), SnO (orange), and metallic Sn (yellow). All TEM scale bars are 100 nm. (For interpretation of the references to colour in this figure legend, the reader is referred to the web version of this article.)

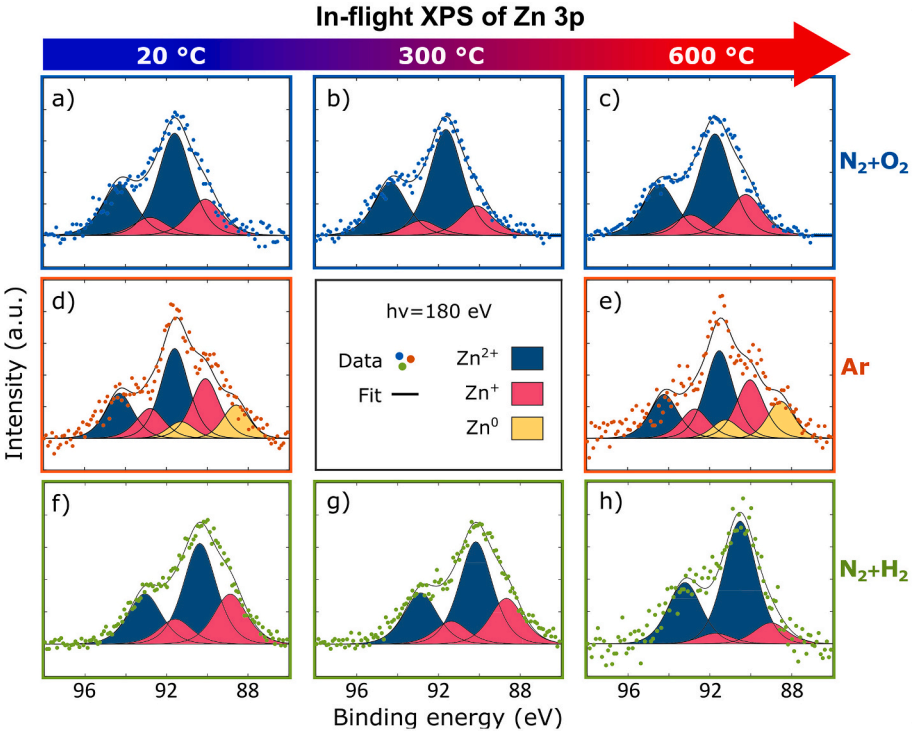

Fig. 7. Zn 3p photoelectron spectra from in-flight XPS of nanoparticles heated at 20 °C (a, d, f), 300 °C (b, g), and 600 °C (c, e, h). The particles were generated by spark ablation of Zn electrodes in different carrier gases: $N_2 + O_2$ (blue), Ar (red), and $N_2 + H_2$ (green), resulting in varying contributions from Zn^{2+}, Zn^{+}, and metallic Zn^0 on the surface. (For interpretation of the references to colour in this figure legend, the reader is referred to the web version of this article.)

(Fig. 7f-h) also can be well fitted by a combination of Zn^{+} and Zn^0, instead of a combination of Zn^{2+} and Zn^{+} as shown here. For transparency, the alternative fits are included Fig. S5. However, the fits presented here agree with the expected ~1 eV shift in peak positions, compared to that in $N_2 + O_2$, when 5% H_2 is added to the carrier gas. Furthermore, the re-oxidation of metallic Zn on the particle surface after exiting the furnace is in line with the results for Sn heated in $N_2 + H_2$ discussed above. The particle morphology when heated in $N_2 + H_2$ and measured using TEM is shown in Fig. 8.

From the TEM images in Fig. 8 of Zn particles produced in $N_2 + H_2$ and heated in-flight at a) 20 °C, b) 300 °C, and c) 600 °C. At room temperature, the TEM images reveal large, dendritic agglomerates composed of relatively large primary particles. As the temperature increases to 300 °C and 600 °C, the structures appear to shrink and become more compact, though not fully spherical. At 600 °C (Fig. 8c), both the agglomerates and its primary particles are noticeably smaller, supporting strong surface evaporation. Thus, under these conditions, the thermodynamic drive for Zn evaporation clearly outweighs that for particle coalescence and compaction. This behaviour is consistent with the size decrease observed in the compaction scans in Fig. 4 where the mobility diameter continued to decrease without reaching a clear plateau up to the highest temperature where particles could still be detected (900 °C), confirming that evaporation, rather than coalescence and compaction, dominates the particle evolution.

From the in-flight XPS results in Fig. 7 it seems like the carrier gas used during particle generation is the primary determinant of Zn surface composition, while subsequent in-flight heating has only minor effects. Previous ZnO annealing studies (using XPS of Zn 2p and O 1 s, and photoluminescence) report conflicting trends regarding vacancy formation. Some observe more vacancies in oxygen-rich atmospheres [63,64], while others report more in inert or reducing atmospheres such as Ar or Ar + H_2 [7,62]. In the present work, a similarly strong Zn^{+} signal, indicative of oxygen vacancies, is found for particles generated in all carrier gases ($N_2 + O_2$, Ar, and $N_2 + H_2$).

The Zn^{2+} $3p_{1/2}$ peak appears between 93 eV and just above 94 eV across all gases and temperatures. This is higher than commonly reported values (91.6–91.5 eV) [65,66] because, unlike standard XPS on grounded samples under ultrahigh vacuum conditions ($<1{\cdot}10^{-8}$ Pa), the present measurements are performed on charged, free nanoparticles in-flight at ($\sim1{\cdot}10^{-4}$ Pa or $1{\cdot}10^{-6}$ mbar). For such suspended particles, binding energies reference the vacuum level rather than the Fermi level, resulting in systematic shifts of approximately the particle work function (~4–5 eV for Sn, Zn, and Al), which is expected relative to literature reference values. A brief discussion on binding-energy alignment in in-

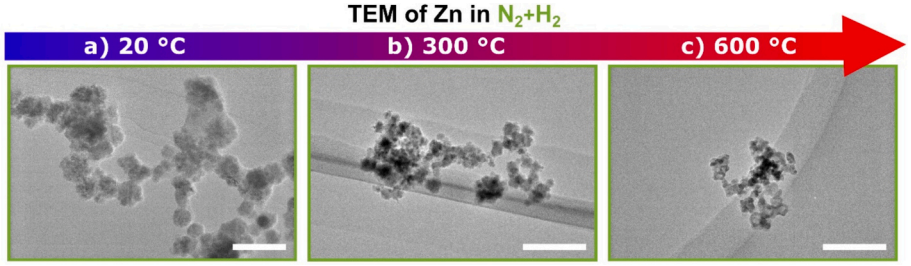

Fig. 8. TEM images of Zn nanoparticles produced in $N_2 + H_2$ and exposed to different temperatures in-flight. Scale bars are 100 nm.

flight XPS is provided in the Supporting Information, with further details in Preger et al. (2025).

3.3.3. Al

Fig. 9 shows the in-flight XPS results for Al nanoparticles generated in $N_2 + O_2$, $Ar + H_2$, and $N_2 + H_2$, and heated in-flight to 20, 500, and 900°. The Al 2p core level was fitted using only the Al^{3+} two spin-orbit components, and all spectra (Fig. 9a-h) show very little variation with gas composition or temperature. No metallic Al is detected. The measured Al 2p binding energies (76–77 eV) are slightly higher than literature values for Al_2O_3 (71–76 eV) [46,67–69], which is reasonable given that the present measurements are performed on charged, suspended particles in-flight rather than on grounded samples.

The peak positions for $N_2 + O_2$ and $N_2 + H_2$, highlighted in blue and green, differ by ~0.5 eV at room temperature, with $N_2 + H_2$ giving the lowest binding energy and $N_2 + O_2$ the highest, about 1 eV above $N_2 + H_2$. Although Al 2p shifts of ~1 eV per oxidation state (+1, +2, +3) have been reported [70], and the observed shift could in principle reflect a transition from Al_2O_3 (Al^{3+}) to AlO (Al^{2+}), a shift in work function caused by the carrier gas environment is also expected. This makes it difficult to distinguish whether the shift arises from oxidation-state changes, work-function differences, or a combination of both.

Upon in-flight heating to 900 °C, the Al 2p peak positions for $N_2 + O_2$ and $Ar + H_2$ remain essentially unchanged, whereas particles generated in $N_2 + H_2$ show a ~ 0.4 eV shift toward higher binding energies. This shift is far smaller than what would be expected for a full oxidation state change, and no peak broadening is observed that would indicate multiple oxidation states on the surface. Fig. 10 shows TEM images of Al generated, and particles heated in-flight up to 900 °C in $N_2 + H_2$. Only minor changes in agglomerate morphology can be seen, in line with the compaction analysis in Fig. 4, suggesting that the particles are already fully oxidized during generation. Therefore, the shift is attributed primarily to a change in electronic work function, though a minor combined contribution cannot be fully excluded.

Recent work has suggested that aluminium nitride (AlN) may form on electrodes during spark ablation in nitrogen-containing gases [71], raising the possibility that the NPs contain AlN. However, the AlN signal lies only ~1 eV below Al-O in the Al 2p region, making it difficult to distinguish from Al-O. The present in-flight XPS data, therefore, cannot confirm or exclude the presence of AlN. While some studies infer AlN from Al 2p alone, its identification is more reliably achieved through N 1 s spectroscopy or XRD [67,69,72–75], which were not performed here.

4. Conclusions

The surface of metal oxide nanoparticles is critical for applications such as gas sensing and catalysis, where high surface area and chemical sensitivity are essential. In this work, in-flight XPS at the MAX IV synchrotron facility was combined with a versatile particle generation method to demonstrate how the surface properties of metal oxide NPs can be tailored by varying the *carrier gas* and *in-flight heating*. Unlike conventional XPS studies, which typically analyse NPs deposited on a substrate, this approach enables both characterization and tuning of NPs while still suspended in the carrier gas, avoiding contamination or substrate interactions. After in-flight optimization, the particles can be deposited onto virtually any substrate for further use. These results emphasize the value of advanced characterization techniques for understanding and controlling nanoparticle surfaces in the gas phase.

The present study investigated three easily oxidized materials: Sn, Zn, and Al. The results show that the surface composition of Sn can be effectively reduced from SnO_2 to SnO and metallic Sn using in-flight heating in a carrier gas containing 5% H_2 (N_2 + 5% H_2), whereas the surface of Al remains largely as Al_2O_3 and is not readily reduced under the gases and temperatures employed. The possible presence of AlN on the nanoparticle surfaces was explored, but could not be confirmed. For Zn, the choice of carrier gas strongly influenced the surface composition, indicating the presence of ZnO, ZnO_x, and Zn, while temperature primarily affected particle compaction and size. The compaction behaviour for all three materials was analysed and related to the surface composition, while the particle size distributions from different gases were related to the estimated average energy per spark, its frequency, and the particle morphology analysed offline by TEM. The results highlight the

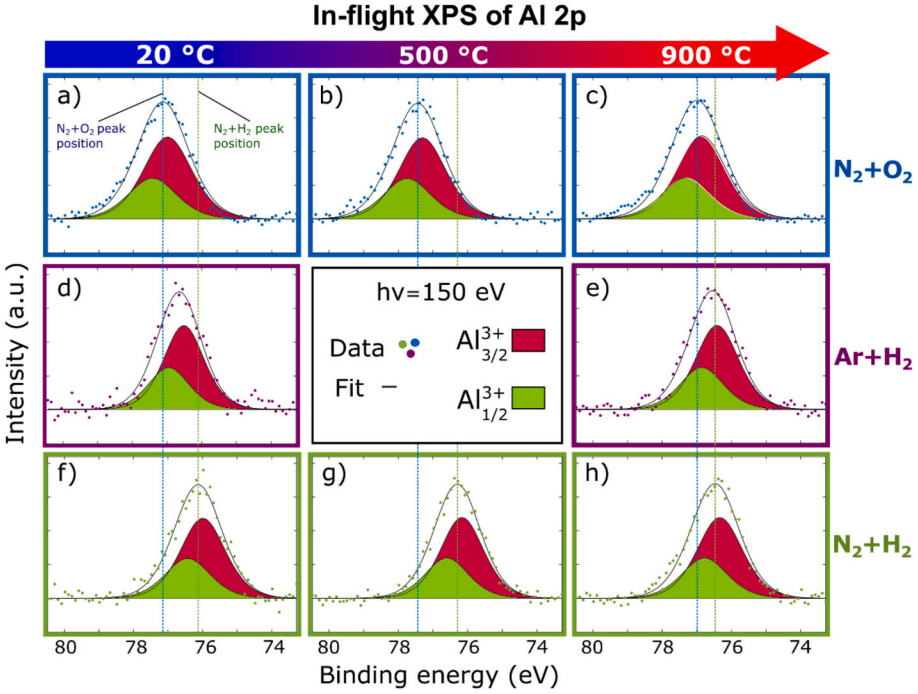

Fig. 9. Al 2p photoelectron spectra from in-flight XPS of nanoparticles made via spark ablation of Al electrodes in $N_2 + O_2$ (blue), $Ar + H_2$ (purple), and $N_2 + H_2$ (green). The particles were heated in-flight to 20 °C (a, d, f), 500 °C (b, g), and 900 °C (c, e, h). Shifts in the Al^{3+} peak positions can be observed depending on the carrier gas and temperature. (For interpretation of the references to colour in this figure legend, the reader is referred to the web version of this article.)

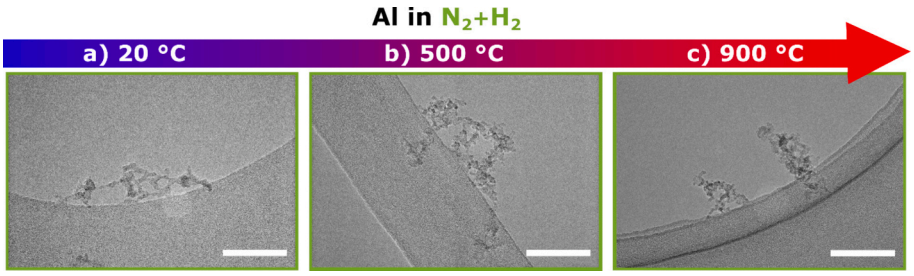

Fig. 10. TEM images of Al nanoparticles produced in N_2 + H_2 and exposed to increasing temperatures in-flight. Scale bars are 100 nm.

importance of studying each material individually to understand and control its properties and enable improved metal oxide-based sensors and catalysts in the future.

CRediT authorship contribution statement

Linnéa Jönsson: Writing – review & editing, Writing – original draft, Visualization, Project administration, Methodology, Investigation, Formal analysis, Data curation, Conceptualization. **Calle Preger:** Writing – review & editing, Supervision, Methodology, Investigation, Formal analysis. **Thomas Krinke:** Writing – review & editing, Supervision, Methodology, Investigation. **Marie Bermeo:** Writing – review & editing, Investigation. **Mehran Sedrpooshan:** Writing – review & editing, Investigation. **Hajar Jalili:** Writing – review & editing, Investigation. **Mohammad Pourhossein:** Writing – review & editing, Investigation. **Bengt O. Meuller:** Writing – review & editing, Investigation. **Axel C. Eriksson:** Writing – review & editing, Investigation. **Jenny Rissler:** Writing – review & editing, Supervision, Investigation. **Knut Deppert:** Writing – review & editing, Supervision, Investigation. **Maria E. Messing:** Writing – review & editing, Supervision, Resources, Funding acquisition, Conceptualization.

Funding

This work was financially supported by the Swedish Foundation for Strategic Research (Grant No. FFL18-0282), the Swedish Research Council (Grant No. 2019-04970 & 201904694), and NanoLund.

Declaration of competing interest

The authors declare that they have no known competing financial interests or personal relationships that could have appeared to influence the work reported in this paper.

Acknowledgement

We acknowledge MAX IV Laboratory for time on Beamline FinEst-BeAMS under Proposal 20240672. Research conducted at MAX IV, a Swedish national user facility, is supported by the Swedish Research Council under contract 2018-07152, the Swedish Governmental Agency for Innovation Systems under contract 2018-04969 and Formas under contract 2019-02496. The Swedish Research Council and Swedish Foundation for Strategic Research are acknowledged for access to nCHREM, which is a part of ARTEMI, the Swedish National Infrastructure in Advanced Electron Microscopy (2021-00171 and RIF210026).

Appendix A. Supplementary data

Supplementary data to this article can be found online at https://doi.org/10.1016/j.powtec.2026.122363.

Data availability

Data will be made available on request.

References

[1] A. Schmidt-Ott, Spark Ablation; Building Blocks for Nanotechnology, Jenny Stanford Publishing, 2019.
[2] A. Efimov, I. Volkov, A. Varfolomeev, A. Vasiliev, V. Ivanov, Tin oxide nanoparticles produced by spark ablation: synthesis and gas sensing properties, Orient. J. Chem. 32 (6) (2016) 2909–2913, https://doi.org/10.13005/ojc/320609.
[3] Y. Sheng, M. Kraft, R. Xu, Emerging applications of nanocatalysts synthesized by flame aerosol processes, Curr. Opin. Chem. Eng. 20 (2018) 39–49, https://doi.org/10.1016/j.coche.2018.01.009.
[4] C. Preger, et al., Controlled oxidation and self-passivation of bimetallic magnetic FeCr and FeMn aerosol nanoparticles, J. Phys. Chem. C 123 (26) (2019) 16083–16090, https://doi.org/10.1021/acs.jpcc.9b01678.
[5] M.K. Kennedy, F.E. Kruis, H. Fissan, B.R. Mehta, S. Stappert, G. Dumpich, Tailored nanoparticle films from monosized tin oxide nanocrystals: particle synthesis, film formation, and sizedependent gas-sensing properties, J. Appl. Phys. 93 (2003) 551–560, https://doi.org/10.1063/1.1525855.
[6] Y. Yoon, P.L. Truong, D. Lee, S.H. Ko, Metal-oxide nanomaterials synthesis and applications in flexible and wearable sensors, ACS Nanosci. Au 2 (2) (2022) 64–92, https://doi.org/10.1021/acsnanoscienceau.1c00029.
[7] A. Ranjbari, K. Demeestere, K.-H. Kim, P.M. Heynderickx, Oxygen vacancy modification of commercial ZnO by hydrogen reduction for the removal of thiabendazole: characterization and kinetic study, Appl. Catal. B Environ. 324 (2023) 122265, https://doi.org/10.1016/j.apcatb.2022.122265.
[8] V.J. Babu, S. Vempati, T. Uyar, S. Ramakrishna, "review of one-dimensional and two-dimensional nanostructured materials for hydrogen generation," (in English), Phys. Chem. Chem. Phys. 17 (5) (2015) 2960–2986, https://doi.org/10.1039/c4cp04245j.
[9] M. Epstein, I. Vishnevetsky, A. Berman, The SnO2/Sn carbothermic cycle for splitting water and production of hydrogen, J. Sol. Energy Eng. 132 (2010) 031007, https://doi.org/10.1115/1.4001403.
[10] S. Drdova, et al., Precursor- and waste-free synthesis of spark-ablated nanoparticles with enhanced photocatalytic activity and stability towards airborne organic pollutant degradation, Environ. Sci. Nano 11 (3) (2024) 1023–1043, https://doi.org/10.1039/d3en00348e.
[11] K. Ki-Joong, P.B. K., A.H. G., C.C. H., Characterization of cotton ball-like au/ZnO photocatalyst synthesized in a micro-reactor, Micromachines 9 (7) (2018) 322, https://doi.org/10.3390/mi9070322.
[12] S. Taghipour, S.M. Hosseini, B. Ataie-Ashtiani, Engineering nanomaterials for water and wastewater treatment: review of classifications, properties and applications, New J. Chem. 43 (21) (2019) 7902–7927, https://doi.org/10.1039/c9nj00157c.
[13] N. Yamazoe, J. Fuchigami, M. Kishikawa, T. Seiyama, Interactions of tin oxide surface with O2, H2O and H2, Surf. Sci. 86 (1979) 335–344, https://doi.org/10.1016/0039-6028(79)90411-4.
[14] T. Hao, G. Cheng, H. Ke, Y. Zhu, Y. Fu, Effects of fluorine ions on the formation and photocatalytic activities of SnO2 nanoparticles with small sizes, RSC Adv. 4 (41) (2014) 21548–21552, https://doi.org/10.1039/c4ra02802c.
[15] Y.K. Gautam, K. Sharma, S. Tyagi, A.K. Ambedkar, M. Chaudhary, B. Pal Singh, Nanostructured metal oxide semiconductor-based sensors for greenhouse gas detection: progress and challenges, R. Soc. Open Sci. 8 (3) (2021) 201324, https://doi.org/10.1098/rsos.201324.
[16] L. Mädler, H.K. Kammler, R. Mueller, S.E. Pratsinis, Controlled synthesis of nanostructured particles by flame spray pyrolysis, J. Aerosol Sci. 33 (2001) 369–389, https://doi.org/10.1016/S0021-8502(01)00159-8.
[17] J. Feng, et al., Green manufacturing of metallic nanoparticles: a facile and universal approach to scaling up, J. Mater. Chem. A 4 (29) (2016) 11222–11227, https://doi.org/10.1039/c6ta03221d.
[18] A. Maisser, K. Barmpounis, M.B. Attoui, G. Biskos, A. Schmidt-Ott, Atomic cluster generation with an atmospheric pressure spark discharge generator, Aerosol Sci. Technol. 49 (10) (2015) 886–894, https://doi.org/10.1080/02786826.2015.1080812.

[19] S. Schwyn, E. Garwin, A. Schmidt-Ott, Aerosol generation by spark discharge, J. Aerosol Sci. 19 (5) (1988) 639–642, https://doi.org/10.1016/0021-8502(88)90215-7.

[20] J. Feng, D. Chen, P.V. Pikhitsa, Y.-H. Jung, J. Yang, M. Choi, Unconventional alloys confined in nanoparticles: building blocks for new matter, Matter 3 (5) (2020) 1646–1663, https://doi.org/10.1016/j.matt.2020.07.027.

[21] S.M. Franzén, et al., Compositional tuning of gas-phase synthesized Pd–cu nanoparticles, Nanoscale Adv. 5 (22) (2023) 6069–6077, https://doi.org/10.1039/d3na00438d.

[22] L. Jönsson *et al.*, "The effect of electrode composition on bimetallic AgAu nanoparticles produced by spark ablation," J. Aerosol Sci., vol. 177, no. 106333, 2024, doi:https://doi.org/10.1016/j.jaerosci.2023.106333.

[23] A. Kohut, et al., Full range tuning of the composition of au/ag binary nanoparticles by spark discharge generation, Sci. Rep. 11 (1) (2021) 5117, 12, https://doi.org/10.1038/s41598-021-84392-6.

[24] R.T. Hallberg, L. Ludvigsson, C. Preger, B.O. Meuller, K.A. Dick, M.E. Messing, Hydrogen-assisted spark discharge generated metal nanoparticles to prevent oxide formation, Aerosol Sci. Technol. 52 (3) (2018) 347–358, https://doi.org/10.1080/02786826.2017.1411580.

[25] A. Maisser, et al., Characterization of atmospheric-pressure spark generated atomic silver and gold clusters by time-of-flight mass spectrometry, J. Aerosol Sci. 156 (2021) 105780, https://doi.org/10.1016/j.jaerosci.2021.105780.

[26] V. Olszok, P. Rembe, A.P. Weber, Aerosol photoemission as a versatile tool for nanoparticle surface investigations: evaluation of metal oxide formation and surface properties of multi-component particles, Aerosol Sci. Technol. 58 (1) (2024) 54–69, https://doi.org/10.1080/02786826.2023.2285307.

[27] V. Olszok, M. Bierwirth, A.P. Weber, Creation of gases with interplanetary oxygen concentration at atmospheric pressure by nanoparticle aerosol scavengers: implications for metal processing from nm to mm range, ACS Appl. Nano Mater. 6 (3) (2023) 1660–1666, https://doi.org/10.1021/acsanm.2c04585.

[28] P.T. Nilsson, et al., In-situ characterization of metal nanoparticles and their organic coatings using laser-vaporization aerosol mass spectrometry, Nano Res. 8 (12) (2015) 3780–3795, https://doi.org/10.1007/s12274-015-0877-9.

[29] A. Kohut, Hydrogen-assisted spark generation of silver nanoparticles: the effect of hydrogen content on the signal intensity in surface-enhanced Raman spectroscopy, J. Aerosol Sci. 167 (2023) 106090, https://doi.org/10.1016/j.jaerosci.2022.106090.

[30] C. Preger, et al., In-flight observation and surface oxidation modification of tin oxide nanoparticles for gas sensing applications, ACS Appl. Nano Mater. 8 (12) (2025) 6004–6013, https://doi.org/10.1021/acsanm.5c00144.

[31] P. Ternero, C. Preger, A.C. Eriksson, J. Rissler, J.M. Hübner, M.E. Messing, In-flight tuning of Au-Sn nanoparticle properties, Langmuir 40 (31) (2024) 16393–16399, https://doi.org/10.1021/acs.langmuir.4c01656.

[32] M. Seipenbusch, A.P. Weber, A. Schiel, G. Kasper, Influence of the gas atmosphere on restructuring and sintering kinetics of nickel and platinum aerosol nanoparticle agglomerates, J. Aerosol Sci. 34 (12) (2003) 1699–1709, https://doi.org/10.1016/S0021-8502(03)00355-0.

[33] M. Snellman, N. Eom, M. Ek, M. E. Messing, K. Deppert, and "Continuous gas-phase synthesis of core-shell nanoparticlesviasurface segregation," Nanoscale Adv., vol. 3, pp. 3041–3052, 6 2021, doi:https://doi.org/10.1039/d0na01061h.

[34] C. Preger, J. Rissler, A. Kivimaki, A.C. Eriksson, N. Walsh, A versatile sample-delivery system for X-ray photoelectron spectroscopy of in-flight aerosols and free nanoparticles at MAX IV Laboratory, J. Synchrotron Radiat. 31 (Pt 5) (2024) 1382–1392, https://doi.org/10.1107/S1600577524005411.

[35] F.X. Ouf, et al., First in-flight synchrotron X-ray absorption and photoemission study of carbon soot nanoparticles, Sci. Rep. 6 (2016) 36495, https://doi.org/10.1038/srep36495.

[36] O. Sublemontier, et al., X-ray photoelectron spectroscopy of isolated nanoparticles, J. Phys. Chem. Lett. 5 (19) (2014) 3399–3403, https://doi.org/10.1021/jz501532c.

[37] Bronkhorst, Gas conversion table, in: Instruction Manual General Instructions Digital Mass Flow / Pressure Instruments Laboratory Style / IN-FLOW, 2024. https://www.bronkhorst.com/int/downloads-1/manuals-and-quick-installation-guides/manual-quick-start-guide-instruments/:Bronkhorst.

[38] B. O. Meuller et al., "Review of spark discharge generators for production of nanoparticle aerosols," Aerosol Sci. Technol., vol. 46, no. 11, pp. 1256–1270, 11 2012, doi:https://doi.org/10.1080/02786826.2012.705448.

[39] A. Kohut, et al., Gold-silver alloy nanoparticle formation via spark ablation: the dynamics of material mixing, Nanoscale Adv. 7 (11) (2025) 3322–3330, https://doi.org/10.1039/d4na01076k.

[40] A. Kohut, G. Galbács, Z. Márton, Z. Geretovszky, Characterization of a copper spark discharge plasma in argon atmosphere used for nanoparticle generation, Plasma Sources Sci. Technol. 26 (4) (2017) 045001, https://doi.org/10.1088/1361-6595/aa5c2b.

[41] N.S. Tabrizi, Q. Xu, N.M. Van Der Pers, A. Schmidt-Ott, Generation of mixed metallic nanoparticles from immiscible metals by spark discharge, J. Nanopart. Res. 12 (1) (2010) 247–259, 1, https://doi.org/10.1007/s11051-009-9603-4.

[42] C. J. P. A. A. Jablonski, NIST Electron Inelastic-Mean-Free-Path Database, Version 1.2, SRD 71, National Institute of Standards and Technology, Gaithersburg, MD, 2010.

[43] O. Dutuit, et al., Critical review of N, N+, N+2, N++, and N++2 main production processes and reactions of relevance to titan's atmosphere, Astrophys. J. Suppl. Ser. 204 (2) (2013) 20, https://doi.org/10.1088/0067-0049/204/2/20.

[44] N. Fairley, et al., Systematic and collaborative approach to problem solving using X-ray photoelectron spectroscopy, Appl. Surf. Sci. Adv. 5 (2021) 100112, https://doi.org/10.1016/j.apsadv.2021.100112.

[45] P. De Padova, M. Fanfoni, R. Larciprete, M. Mangiantini, S. Priori, P. Perfetti, A synchrotron radiation photoemission study of the oxidation of tin, Surf. Sci. 313 (3) (1994) 379–391, https://doi.org/10.1016/0039-6028(94)90058-2.

[46] A.J. Lizarbe, G.H. Major, V. Fernandez, N. Fairley, M.R. Linford, Insight note: X-ray photoelectron spectroscopy (XPS) peak fitting of the Al 2p peak from electrically isolated aluminum foil with an oxide layer, Surf. Interface Anal. 55 (9) (2023) 651–657, https://doi.org/10.1002/sia.7238.

[47] J.W. Pinder, et al., Avoiding common errors in X-ray photoelectron spectroscopy data collection and analysis, and properly reporting instrument parameters, Appl. Surf. Sci. Adv. 19 (2024) 100534, https://doi.org/10.1016/j.apsadv.2023.100534.

[48] P. Samuelsson, "Towards Optical Diagnostics and Control in Aerotaxy Semiconductor Nanowire Growth," Doctor, PhD Thesis, Department of Physics, Lund University, 2021.

[49] J.M. Palomares, A. Kohut, G. Galbács, R. Engeln, Z. Geretovszky, A time-resolved imaging and electrical study on a high current atmospheric pressure spark discharge, J. Appl. Phys. 118 (2015) 233305, https://doi.org/10.1063/1.4937729.

[50] N.S. Tabrizi, M. Ullmann, V.A. Vons, U. Lafont, A. Schmidt-Ott, Generation of nanoparticles by spark discharge, J. Nanopart. Res. 11 (2) (2009) 315–332, https://doi.org/10.1007/s11051-008-9407-y.

[51] M. Stein, D. Kiesler, F.E. Kruis, Effect of carrier gas composition on transferred arc metal nanoparticle synthesis, J. Nanopart. Res. 15 (1) (2013) 1400, https://doi.org/10.1007/s11051-012-1400-9.

[52] A.P. Weber, S.K. Friedlander, In situ determination of the activation energy for restructuring of nanometer aerosol agglomerates, J. Aerosol Sci. 28 (2) (1997) 179–192, https://doi.org/10.1016/S0021-8502(96)00062-6.

[53] V. Olszok, M. Bierwirth, A.P. Weber, Interaction of reactive gases with platinum aerosol particles at room temperature: effects on morphology and surface properties, Nanomaterials 11 (9) (2021) 2266, https://doi.org/10.3390/nano11092266.

[54] M.N.A. Karlsson, K. Deppert, S.L. Karlsson, M.H. Magnusson, J.-O. Malm, N. S. Srinivasan, Compaction of agglomerates of aerosol nanoparticles: A compilation of experimental data, J. Nanopart. Res. 7 (2005) 43–49, https://doi.org/10.1007/s11051-004-7218-3.

[55] M.H. Magnusson, K. Deppert, J.-O. Malm, J.-O. Bovin, L. Samuelson, Gold nanoparticles: production, reshaping, and thermal charging, J. Nanopart. Res. 1 (2) (1999) 243–251, https://doi.org/10.1023/A:1010012802415.

[56] C.B. Alcock, V.P. Itkin, M.K. Horrigan, Vapour pressure equations for the metallic elements: 298–2500K, Can. Metall. Q. 23 (3) (1984) 309–313, https://doi.org/10.1179/cmq.1984.23.3.309.

[57] M. Snellman, N. Eom, M.E. Messing, K. Deppert, A thermal evaporator for aerosol core-shell nanoparticle synthesis, J. Aerosol Sci. 175 (2024) 106276, https://doi.org/10.1016/j.jaerosci.2023.106276.

[58] T. Wojtal, The influence on temperature on the speed of reduction of tin oxide with argon hydrogen mixture, Metalurgija 61 (3–4) (2022) 653–656.

[59] I. Resa, E. Carmona, E. Gutierrez-Puebla, A. Monge, Decamethyldizincocene, a stable compound of Zn(I) with aZn–Zn bond, Science 305 (5687) (2004) 1136–1138.

[60] E. Ciftyurek, Z. Li, K. Schierbaum, Engineered porosity ZnO sensor enriched with oxygen vacancies enabled extraordinary sub-ppm sensing of hydrogen sulfide and nitrogen dioxide air pollution gases at low temperature in air, Sensors 24 (23) (2024), https://doi.org/10.3390/s24237694.

[61] L. Cui, et al., Effect of annealing temperature and annealing atmosphere on the structure and optical properties of ZnO thin films on sapphire (0001) substrates by magnetron sputtering, Appl. Surf. Sci. 258 (7) (2012) 2479–2485, https://doi.org/10.1016/j.apsusc.2011.10.076.

[62] Y. Zhang, et al., Effect of annealing atmosphere on the photoluminescence of ZnO nanospheres, Appl. Surf. Sci. 255 (9) (2009) 4801–4805, https://doi.org/10.1016/j.apsusc.2008.11.091.

[63] F.M. Chang, S. Brahma, J.H. Huang, Z.Z. Wu, K.Y. Lo, Strong correlation between optical properties and mechanism in deficiency of normalized self-assembly ZnO nanorods, Sci. Rep. 9 (1) (2019) 905, https://doi.org/10.1038/s41598-018-37601-8.

[64] I.M. Hegazy, R.A. Geioushy, S.M. El-Sheikh, A. Shawky, S. El-Sherbiny, A.-H. T. Kandil, Influence of oxygen vacancies on the performance of ZnO nanoparticles towards CO2 photoreduction in different aqueous solutions, J. Environ. Chem. Eng. 8 (4) (2020) 103887, https://doi.org/10.1016/j.jece.2020.103887.

[65] L. Bigiani, A. Gasparotto, G. Carraro, C. Maccato, D. Barreca, ZnO-based nanocomposites prepared by a vapor phase route, investigated by XPS, Surf. Sci. Spectra 25 (2018) 024005, https://doi.org/10.1116/1.5048909.

[66] B.J.A. José, M.D. Shinde, Colloidal stability and dielectric behavior of eco-friendly synthesized zinc oxide nanostructures from Moringa seeds, Sci. Rep. 14 (1) (2024) 2310, https://doi.org/10.1038/s41598-024-52093-5.

[67] M. Alizadeh, et al., Plasma-assisted hot filament chemical vapor deposition of AlN thin films on ZnO buffer layer: toward highly c-axis-oriented, uniform, insulative films, Appl. Phys. A Mater. Sci. Process. 117 (4) (2014) 2217–2224, https://doi.org/10.1007/s00339-014-8649-z.

[68] L. Sun, et al., Effects of post annealing treatments on the interfacial chemical properties and band alignment of AlN/Si structure prepared by atomic layer deposition, Nanoscale Res. Lett. 12 (1) (2017) 102, https://doi.org/10.1186/s11671-016-1822-x.

[69] W.O. Èsterle, I.D. Èrfel, I. Urban, T. Reier, J.W. Schultze, XPS and XTEM study of AlN formation by N+2 implantation of aluminium, Surf. Coat. Technol. 102 (1998) 168–174, https://doi.org/10.1016/S0257-8972(98)00355-7.

[70] S. Kurumada, et al., Mechanochemical synthesis of non-solvated dialkylalumanyl anion and XPS characterization of Al(I) and Al(II) species, Chemistry 30 (7) (2024), https://doi.org/10.1002/chem.202303073 p. e202303073.

[71] K.C. Petallidou, A. Schmidt-Ott, G. Biskos, Stability of nanoparticle production by atmospheric-pressure spark ablation, Aerosol Sci. Technol. 58 (9) (2024) 1079–1088, https://doi.org/10.1080/02786826.2024.2347999. Art no. 9.
[72] H. Kim, N.D. Kim, S.C. An, B.J. Choi, Electrical characteristics of atomic layer deposited AlN on n-InP, J. Mater. Sci. Mater. Electron. 29 (20) (2018) 17508–17516, https://doi.org/10.1007/s10854-018-9851-0.
[73] A. Mahmood, et al., Optical and surface analysis of DC-reactive sputtered AlN films, Diam. Relat. Mater. 12 (8) (2003) 1315–1321, https://doi.org/10.1016/s0925-9635(03)00076-1.
[74] D. Manova, V. Dimitrovaa, D. Karpuzovb, R. Yankovc, Reactively DC magnetron sputtered thin AlN films studied by X-ray photoelectron spectroscopy and polarised infrared reflection, Vacuum 52 (1999) 301–305, https://doi.org/10.1016/s0042-207x(98)00303-0.
[75] P. Motamedi, K. Cadien, XPS analysis of AlN thin films deposited by plasma enhanced atomic layer deposition, Appl. Surf. Sci. 315 (2014) 104–109, https://doi.org/10.1016/j.apsusc.2014.07.105.